PROCEEDINGS A

rspa.royalsocietypublishing.org

Research

Cite this article: Turangan CK, Ball GJ, Jamaluddin AR, Leighton TG. 2017 Numerical studies of cavitation erosion on an elastic–plastic material caused by shock-induced bubble collapse. *Proc. R. Soc. A* **473**: 20170315.
http://dx.doi.org/10.1098/rspa.2017.0315

Received: 15 May 2017
Accepted: 11 August 2017

Subject Areas:
acoustics, fluid mechanics, computer modelling and simulation

Keywords:
shock-induced bubble collapse, high-speed liquid impact, lithotripsy, free-Lagrange method

Author for correspondence:
C. K. Turangan
e-mail: cary@ihpc.a-star.edu.sg

†Present address: Romax Technology Ltd, Nottingham Science and Technology Park, Nottingham NG7 2PZ, UK

Electronic supplementary material is available online at https://dx.doi.org/10.6084/m9.figshare.c.3865480.

THE ROYAL SOCIETY PUBLISHING

Numerical studies of cavitation erosion on an elastic–plastic material caused by shock-induced bubble collapse

C. K. Turangan[1], G. J. Ball[2], A. R. Jamaluddin[3,†] and T. G. Leighton[3,4]

[1]Department of Fluid Dynamics, Institute of High Performance Computing, Singapore 138632
[2]Atomic Weapons Establishment, Aldermaston, Reading RG7 4PR, UK
[3]Faculty of Engineering and the Environment, and [4]Institute of Sound and Vibration Research, University of Southampton, Highfield, Southampton SO17 1BJ, UK

CKT, 0000-0003-3926-2369

We present a study of shock-induced collapse of single bubbles near/attached to an elastic–plastic solid using the free-Lagrange method, which forms the latest part of our shock-induced collapse studies. We simulated the collapse of 40 µm radius single bubbles near/attached to rigid and aluminium walls by a 60 MPa lithotripter shock for various scenarios based on bubble–wall separations, and the collapse of a 255 µm radius bubble attached to aluminium foil with a 65 MPa lithotripter shock. The coupling of the multi-phases, compressibility, axisymmetric geometry and elastic–plastic material model within a single solver has enabled us to examine the impingement of high-speed liquid jets from the shock-induced collapsing bubbles, which imposes an extreme compression in the aluminium that leads to pitting and plastic deformation. For certain scenarios, instead of the high-speed jet, a radially inwards flow along the aluminium surface contracts the bubble to produce a 'mushroom shape'. This work provides methods for quantifying which parameters (e.g. bubble sizes and separations from the solid) might promote or inhibit erosion on solid surfaces.

1. Introduction

Shock-induced collapse of gas-filled cavitation bubbles, which results in the formation and impingement of high-speed liquid jets, is an extremely violent event. Depending on the shock strength, the jet velocity can reach over 1 km s^{-1} [1–5], which is about 10 times higher than the typical velocity of jets from the inertial collapse of bubbles near solid walls [6]. If the bubbles reside very close to or are attached to solid walls, the jet velocity can reach high subsonic or even supersonic speed because of the additional compression of the bubble by the shock reflected by the walls [3]. The jet impact on the solid wall imposes a high stress and strain liquid motion that leads to solid erosion, and eventually substantial damage if the number of bubbles is high. The pressures generated in the blast wave after jet impact can reach a few gigapascal [1–5], which further contributes to the overall depression in the solid.

In general, bubble collapse (either shock-induced or inertial) has relevance in the surface erosion of fluid machinery [7], underwater explosions [8], kidney stone fragmentation during shockwave lithotripsy (SWL) [4,9] and sensitization of explosives through hotspots [10,11]. For biomedical applications, jetting collapse of cavitation bubbles may offer possibilities of *in vivo* local drug delivery by means of a micro-syringe from bubbles loaded with therapeutic agents [12]. It has also been explored for sonolysis of *Escherichia coli* and *Pichia pastoris* bacteria [13]. However, simply knowing that jetting can be produced is not sufficient because we must also have reliable quantitative methods for predicting where, under what conditions and how violently it will occur. For example, while the ability of such cavitation to destroy cells is valuable for such purposes, if we wish to clean using cavitation without destroying valuable cells (e.g. in ultrasonic cleaning of teeth [14,15] (also see the electronic supplementary material) or hands [16]), it is also important to be able to predict which acoustic fields might generate cleaning by bubble activity without damaging other tissues in the vicinity.

While cavitation jets deforming and puncturing a material have been attributed as: the cause of punctures in aluminium foil that has for decades been the favoured proxy used by industry to predict the cleaning potential of a given ultrasonic bath; a possible way to inject drugs into tissue; the cause of pit formation in structures ranging from marine propellers to mercury containment facilities in pulsed neutron sources, there have never been any shock-induced bubble collapse simulations showing this effect. This paper provides this. Furthermore, it provides methods for quantifying which bubble sizes, separations from the solid and pulse profiles might promote or inhibit erosion, as these cases (ranging from ship or nuclear to biomedical engineering) require.

In experiments, shock-induced bubble collapse has been studied extensively by means of 'gas discs' cast in a water–gelatin sheet, which are collapsed with a shockwave from a high-speed impactor [1,17]. A similar technique has been adopted elsewhere [18], in which a strong shockwave (e.g. greater than 100 MPa) was generated to collapse a bubble (2.5 mm radius) to examine the light emission during the collapse. Kodama & Takayama [19] proposed a method in which a small bubble (0.12–3.06 mm radius) placed near solid gelatin in water was collapsed with the spherical shockwave (10.2 ± 0.5 MPa peak pressure) generated from a laser-induced breakdown. Philipp *et al.* [20] also investigated the interaction of small bubbles (0.15–1.2 mm radius) attached to a 25 µm thick polypropylene foil with a 65 MPa peak pressure lithotripter shock, which is of our particular interest, and with which a qualitative comparison has been made and presented here. Experimental observation is, however, very challenging even with the use of high-speed photography owing to the small spatial and temporal resolution of the collapse events.

Shock-induced bubble collapse involves interconnecting aspects such as compressibility, shock propagation and multi-phases in a highly transient environment, which must be incorporated in the numerical schemes for its simulations. Ball *et al.* [2] simulated the collapse of a 6 mm diameter cylindrical air bubble by a 1.9 GPa shock using the free-Lagrange method (FLM) to study how the bubble evolves and to examine the thermal characteristics of the collapse events. This work established a methodology for our previous studies in which the FLM was further

developed to include the axisymmetric geometry for the asymmetric collapse of inertial spherical bubbles near rigid/aluminium walls, the shock-induced collapse of 40 µm radius bubbles in a free field and near a rigid wall, and the coupling of the FLM with the Kirchhoff/Ffowcs William–Hawkings formulations to predict the far-field acoustic signatures from the collapse of single/cavitation clouds for the development of a clinical device used during lithotripsy [3,4, 21,22]. Other schemes used for shock-induced bubble collapse simulations include the arbitrary Lagrangian–Eulerian [23], level set [24], weighted essentially non-oscillatory scheme [25], front tracking [5], ghost fluid [26] and boundary element methods (BEM) [27] (see [4,5] for a review). For inertial collapse (i.e. underwater explosion type), the BEM has been one of the most popular schemes [6,28,29].

The simulations by these schemes with their respective advantages have undoubtedly revealed many of the key characteristics of collapse events, including the complex shock propagation and interaction inside a bubble and the surrounding liquid, which have been otherwise overlooked in experiments. However, most of these simulations were performed to advance our understanding only in the fluid dynamics aspects associated with the collapse in a free field or near a rigid wall. However, to quantitatively predict the erosion associated with cavitation, the walls must represent real materials whereby the response and the potential damage to the materials can be correctly quantified. As demonstrated in our previous works [3,4], it is the bubbles located very near to a wall that are of particular interest because the presence of the wall has a significant contribution to how violent the collapse can be by inducing a faster jet and higher pressures in the blast wave.

There have been several attempts to simulate the shock-induced collapse of bubbles near physical wall models. Freund *et al.* [30] simulated the collapse of a 20 µm diameter air bubble with a 40 MPa shock near a 'tissue' modelled as a viscous liquid. They showed the progressive motion of the 'tissue' in response to jet impingement, but did not incorporate any structural damage mechanism. Xie & Young [31] also simulated the collapse of a two-dimensional gas bubble by a 2 GPa shock near a semi-infinite deformable solid. The incident shock and the blast wave propagation in the solid were shown without quantifying the solid deformation. Chahine and Hsiao [32,33] and Hsiao *et al.* [34] carried out numerical studies to investigate the solid material erosion caused by the inertial collapse of cavitation bubbles using a hybrid approach: the incompressible BEM code (to capture the bubble dynamics) was coupled with a finite difference code (to quantify the liquid pressures from the collapse events) and a finite element code (to model the solid deformation).

The FLM used in this work introduced the ability to simulate the bubble response after the jet impacts the downstream bubble wall, and so predicted the blast wave generated by this [2]. This blast wave contained pressures far in excess of those which occur prior to jet impact, and so the FLM revealed and quantified what is probably the main damage mechanism for solids near such collapses. However, until this paper, the FLM could not predict damage from such collapses because it has not incorporated multi-phases [2,35], the elastic–perfectly plastic response of solids subjected to extreme loading through the incorporation of elastic–plastic material models [35,36] and axisymmetric geometry [3,4,21,37]. This paper incorporates these features within a single solver to illustrate the versatility of the technique for simulating highly transient and deforming multi-phase flows that involve extensive material distortion in solids. This paper aims to allow damage predictions for applications ranging from erosion problems from a century ago [7] to modern ones in neutron generation facilities [38–40], and from opportunities in drug delivery [12] to those in cleaning [16], by simulating the shock-induced collapse of single bubbles attached to rigid and to elastic–plastic solids so as to examine the solid deformation associated with the jetting collapse of the bubbles for various scenarios.

2. Free-Lagrange numerical scheme with an elastic–plastic numerical model

The Riemann-based free-Lagrange scheme Vucalm solves the unsteady and compressible Euler equations derived from the conservation laws for continuous media in a Lagrangian reference

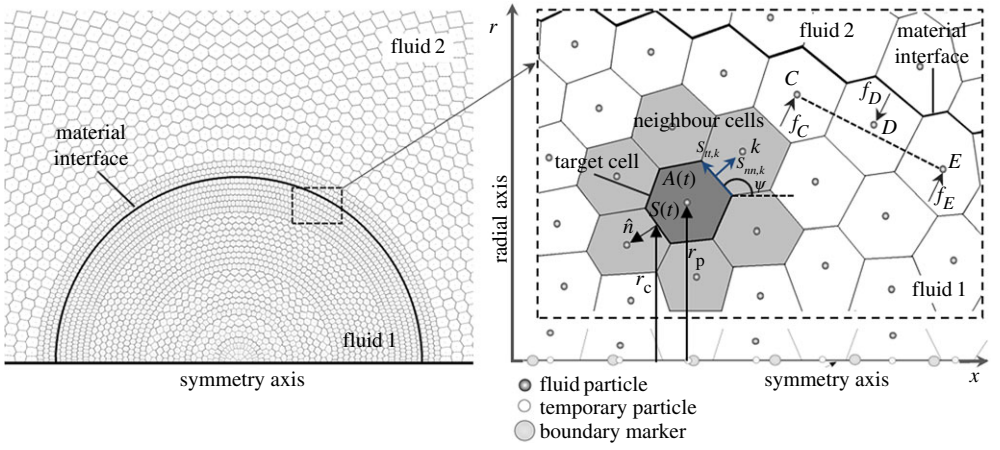

Figure 1. Voronoi mesh used in the simulations. Each cell is a control volume that encloses a single cell-centred particle. It carries an individual fluid type and is bounded by K cell boundaries that represent K neighbours. Material interfaces always coincide with cell boundaries and no mass transfer is permitted across the interfaces. To update the flow variables (ρ, u, v, T), numerical fluxes across cell boundaries are determined using Riemann solvers of the Godunov type. The construction of the edge-oriented normal and tangential stresses for neighbour k (i.e. $s_{nn,k}$, $s_{tt,k}$) is illustrated where ψ is the angle between the cell face and the positive x-axis. An artificial surface tension (an interface smoothing algorithm; for details see [4,35]) is implemented by applying restoring forces f_C, f_D and f_E to particles C, D and E, respectively, so as to move particle D towards an imaginary line joining particles C and E. (Online version in colour.)

frame. The scheme has been well described for two-dimensional planar geometries [2,35,41], including those of the elastic–plastic material model [36]. For axisymmetric geometries, however, the scheme was only partially described in our earlier works [3,4,21,37]. As the present work focuses more on the mechanisms of solid material deformation associated with bubble jetting, in which the axisymmetric form of the scheme and the elastic–plastic material model are the keys ingredients, the free-Lagrange scheme is (briefly) elaborated as follows. The swirl-free axisymmetric form of the scheme that incorporates the elastic–perfectly plastic flow model is written as

$$\frac{\partial}{\partial t}\int_{A(t)} \bar{U}(r_p\,\mathrm{d}A) + \oint_{S(t)} \hat{n}\cdot\bar{F}(r_c\,\mathrm{d}S) = \int_{A(t)} \bar{G}(r_p\,\mathrm{d}A) - \int_{A(t)} \bar{H}(r_p\,\mathrm{d}A). \tag{2.1}$$

The vectors of the conserved variables $\bar{U}$, flux $\bar{F}$ (consists of the hydrodynamic flux $\bar{F}_h$ for pressure distribution on the control volume and the deviatoric flux $\bar{F}_s$ for deviatoric stresses acting on the control volume) and source terms $\bar{G}$ and $\bar{H}$ associated with the axisymmetric geometry are

$$\bar{U} = \begin{bmatrix} 1 \\ \rho\bar{u} \\ \rho E \end{bmatrix}, \quad \bar{F} = \begin{bmatrix} -\bar{u} \\ \underline{I}p - \underline{s} \\ \bar{u}p - \bar{u}\cdot\underline{s} \end{bmatrix}, \quad \bar{G} = \begin{bmatrix} 0 \\ \dfrac{\bar{e}_r P_f}{r_p} \\ 0 \end{bmatrix} \quad \text{and} \quad \bar{H} = \begin{bmatrix} 0 \\ \dfrac{\bar{e}_r s_{\theta\theta}}{r_p} \\ 0 \end{bmatrix}. \tag{2.2}$$

The variables are described with respect to figure 1, which illustrates the unstructured Voronoi mesh used to discretize the computational domain. Each cell represents a control volume that encloses an individual particle and is bounded by cell boundaries. The time-dependent variables $A(t)$ and $S(t)$ are the area and boundary length of the cell, r_p and r_c are the radial distances of the particle and the cell boundary from the symmetry axis, respectively, $\hat{n}$ is the unit normal vector of the cell boundary, ρ is the fluid density, $\bar{u}$ is the fluid velocity ($\bar{u} = (u, v)$, where u and v are the velocity components in the symmetry axis (x) and radial axis (r), respectively), E is the energy per unit mass ($E = \varepsilon + (\bar{u}\cdot\bar{u})/2$, where ε is the internal energy), $\underline{I}$ is the unit tensor, p is the static pressure, $\bar{e}_r$ is the unit radial vector and P_f is the pressure acting on a control

volume for the axisymmetric formulation. The deviatoric stress tensor $\underline{s}$ has four components: the normal stresses in the axial and radial directions (s_{xx} and s_{rr}), the shear stress (s_{xr}) and the stress in the circumferential direction, also known as the hoop stress ($s_{\theta\theta}$). At the beginning of the simulations, each particle is prescribed with thermodynamic conditions, initial conditions and coordinates.

Using the operator time-splitting technique [36], the governing equation (2.1) can be split into the hydrodynamic and deviatoric operators, respectively, i.e.

$$\frac{\partial}{\partial t}\int_{A(t)} \bar{U}(r_\mathrm{p}\,\mathrm{d}A) + \oint_{S(t)} \hat{n}\cdot\bar{F}_\mathrm{h}(r_\mathrm{c}\,\mathrm{d}S) = \int_{A(t)} \bar{G}(r_\mathrm{p}\,\mathrm{d}A) \tag{2.3}$$

and

$$\frac{\partial}{\partial t}\int_{A(t)} \tilde{\bar{U}}(r_\mathrm{p}\,\mathrm{d}A) + \oint_{S(t)} \hat{n}\cdot\bar{F}_\mathrm{s}(r_\mathrm{c}\,\mathrm{d}S) = -\int_{A(t)} \bar{H}(r_\mathrm{p}\,\mathrm{d}A), \tag{2.4}$$

which are solved sequentially over a single time step to update the flow variables and the stresses. The vectors $\bar{F}_\mathrm{h} = [-\bar{u}\ \underline{I}p\ \bar{u}p]^\mathrm{T}$ and $\bar{F}_\mathrm{s} = [0\ -\underline{s}\ -\bar{u}\cdot\underline{s}]^\mathrm{T}$ are the hydrodynamic and deviatoric fluxes, respectively, and $\tilde{\bar{U}}$ is the intermediate value of the conserved variable vector from the solution of equation (2.3). If the medium is not an elastic–plastic solid, the solution of the flow variables from the hydrodynamic operator (2.3) becomes the final values in the new time level. Otherwise, the solution of the flow variables represents the intermediate values of the flow variables, which become the inputs for the deviatoric operator (2.4).

For the axisymmetric geometry of the hydrodynamic operator, the computational cell volume for 1 rad rotation is $V = r_\mathrm{p}\,\mathrm{d}A = m/\rho$, where m is the mass of the computational cell. For a K-sided polygonal computational cell, equation (2.3) can be written in terms of the present nth and the intermediate time levels to give

$$\tilde{\bar{U}} = \frac{\tilde{\rho}}{\rho^n}\left[\bar{U}^n - \frac{\rho^n \Delta t}{m}\sum_{k=1}^{K} \hat{n}_k\cdot\bar{F}^n_{h,k}(r_{\mathrm{c},k}S_k) + \bar{G}\Delta t\right], \tag{2.5}$$

where

$$\bar{F}_{h,k} = (A_I)\bar{F}^*_{h,k}, \quad A_I = \begin{bmatrix} \hat{n} & 0 & 0 \\ 0 & \underline{I} & 0 \\ 0 & 0 & \hat{n} \end{bmatrix}, \quad \bar{F}^*_{h,k} = \begin{bmatrix} -u^*_k \\ p^*_k \\ u^*_k p^*_k \end{bmatrix}. \tag{2.6}$$

The cell boundary always coincides with the contact surface of the local Riemann problem in a Lagrangian mesh. Therefore, the flow variables (ρ,u,v,T) are updated using equation (2.5) by computing the numerical flux $\bar{F}_{h,k}$ on the kth side of the cell. This is done by solving the one-dimensional Riemann problem on the kth side of the cell boundary to obtain the wave-processed variables (velocity u^*_k and pressure p^*_k) for all cell sides using Riemann solvers of the Godunov type [41]. A nominal second-order spatial accuracy is achieved using a piecewise-linear reconstruction of the flow variables with a MUSCL-based slope limiter [42]. The three types of Riemann solvers adapted to FLM code [2,36,41] are: the HLLC approximate solver for air–air interfaces, the Riemann solver proposed by Flores & Holt [2,43] for air–water and water–water interfaces, and the non-iterative approximate solver proposed by Dukowicz [44] for solid–solid, solid–air and solid–water interfaces. Dukowicz's Riemann solver can also be used for air–water and water–water interfaces.

The evaluation of the flow variables in the deviatoric step is similar to that of the hydrodynamic step [36],

$$\bar{U}^{n+1} = \frac{\tilde{\rho}}{\rho^n}\left[\tilde{\bar{U}} - \frac{\rho^n \Delta t}{m}\sum_{k=1}^{K} \hat{n}_k\cdot\bar{F}^n_{s,k}(r_{\mathrm{c},k}S_k) - \bar{H}\Delta t\right], \tag{2.7}$$

where

$$\bar{F}_{s,k} = \begin{bmatrix} 0 \\ -n_x s_{nn,k} + n_r s_{tt,k} \\ -n_r s_{nn,k} - n_x s_{tt,k} \\ -u_k^* s_{nn,k} - u_{tt} s_{tt,k} \end{bmatrix} \quad \text{and} \quad \bar{H} = \begin{bmatrix} 0 \\ 0 \\ \dfrac{\bar{e}_r s_{\theta\theta}}{r_p} \\ 0 \end{bmatrix}. \tag{2.8}$$

The variables n_x and n_r are the axial and radial components of unit normal vector $\hat{n}_k$ acting on the kth cell boundary, respectively, and u_k^* and u_{tt} are the velocities normal and tangential to the kth cell boundary, respectively. As illustrated in figure 1, $s_{nn,k}$ and $s_{tt,k}$ are the edge-oriented normal and tangential stresses, respectively, which are functions of angle ψ, and are used to update s_{xx}, s_{rr} and s_{xr} [36]. To evaluate $s_{\theta\theta}$, its time derivative is considered to be [45]

$$\dot{s}_{\theta\theta} = 2\mu \left(\dot{\epsilon}_{\theta\theta} - \frac{1}{3} \frac{\dot{\nu}}{\nu} \right), \tag{2.9}$$

where μ is the shear modulus of the material of interest and $\dot{\epsilon}_{\theta\theta}$ is the time derivative of the strain in the circumferential direction ($\dot{\epsilon}_{\theta\theta} = \dot{r}/r$, where r is the radial distance of the centre of the computational cell from the symmetry axis, $\dot{r} = v$ is the radial velocity), ν is the specific volume and $\dot{\nu}/\nu = \dot{\epsilon}_{xx} + \dot{\epsilon}_{rr} + \dot{\epsilon}_{\theta\theta}$ is obtained from the consideration of continuity, where $\dot{\epsilon}_{xx}$ and $\dot{\epsilon}_{rr}$ are time derivatives of normal strains in the axial x and radial r directions, respectively. Equation (2.9) can be integrated in time to give the hoop stress $s_{\theta\theta}$ at the new time level, i.e.

$$s_{\theta\theta}^{n+1} = s_{\theta\theta}^{n} + [2\mu(\dot{\epsilon}_{\theta\theta} - \tfrac{1}{3}(\dot{\epsilon}_{xx} + \dot{\epsilon}_{rr} + \dot{\epsilon}_{\theta\theta}))]\Delta t. \tag{2.10}$$

Before the updated state of the deviatoric stresses is accepted as the final stress value of the material under consideration, it must be tested against the yield condition, and for which the von Mises yield condition implemented using the method of radial return is adopted. The von Mises yield condition stated in two-dimensional axisymmetric fixed deviatoric space [45] is given by

$$s_{xx}^2 + s_{rr}^2 + s_{\theta\theta}^2 + 2s_{xr}^2 \leq \tfrac{2}{3}(Y_0)^2, \tag{2.11}$$

where Y_0 is the yield strength of the material of interest, which must be calculated to determine the elastic–plastic yield of the material. The elastic–perfectly plastic model of a given solid material (assumed to be continuous, homogeneous and isotropic) follows the work-hardening model. The stress is to increase linearly as a function of strain. If the load is released before reaching the material's yield point, the stress returns to its original value and the material is said to be in the elastic regime. Beyond that point, the stress will remain constant and equal to the yield point, and the material is considered to flow plastically whereby a permanent deformation occurs [36].

Regarding the equation of state (EOS), air is represented by the ideal gas EOS (i.e. $p = \rho RT$, where p is pressure, ρ is density, $R = 287.14\,\mathrm{J\,kg^{-1}\,K}$ is the gas constant for air and T is temperature), and water by the Tait EOS (i.e. $p = B[(\rho/\rho_R)^\eta - 1]$, where $\rho_R = 999.96\,\mathrm{kg\,m^{-3}}$ is the reference density and $B = 3.31 \times 10^8$ Pa and $\eta = 7$ are constants). The application of these EOSs in the present work is based on some assumptions, and their validity and limitations have been discussed by Ball *et al.* [2]. For solids (e.g. aluminium), the Osborne EOS, which takes the form of a quadratic fit to experimental data, is employed (see [36] for the detailed formulation). Here, the heat and mass transfer, viscosity and surface tension have been omitted. The temperature is calculated for the air phase only, which then tends to overestimate the prediction of temperature inside the bubble. It was argued that the dynamics of the bubble is dominated by the water inertia [2] and the time scale for the main events of the collapse is very short. Therefore, the significant extra computational load taken to include these aspects was not, with current resources, considered commensurate with the extra accuracy they would bring. Additionally, owing to the formulation in axisymmetric geometry, the three-dimensional effects of the flow are not captured.

3. Lithotripter shock-induced bubble collapse simulations

(a) A single bubble attached to a planar rigid wall

Jamaluddin *et al*. [4] simulated the collapse of a single 40 µm radius air bubble near a rigid wall by a 60 MPa lithotripter shock for different stand-off distances. The aim was to assess the role of wall distance in the dynamics of the collapse. The 40 µm radius is typical of secondary stable bubbles that have been formed as a result of the interaction of a cavitation nucleus with a preceding lithotripter shock [46]. Jamaluddin *et al.* found that the presence of the wall seemed to elongate the bubble during collapse. It also increased the jet velocity (and the resulting pressure from the blast wave), which then produced a more violent collapse than when the bubble is in a free field. A question that becomes the impetus for the present work is: What is the collapse like if the bubble is attached to the wall? Apart from the work by Lauer *et al.* [47], who simulated the collapse of a pre-attached bubble on a rigid wall by a pressure difference between the surrounding liquid and the bubble, i.e. an instantaneous collapse of the 'Rayleigh collapse' type, the shock-induced collapse of cavitation bubbles initially attached to solid walls has been surprisingly overlooked.

In our present numerical studies, the 60 MPa lithotripter shock is used (to be consistent with our previous works [4,21]), whose analytical expression is given by

$$P_s(t) = 2P^+ \, e^{-\alpha_d t} \cos\left(\omega t + \frac{\pi}{C_o}\right), \tag{3.1}$$

where $P^+ = 60$ MPa is the peak pressure (at $t = 0$, $P_s = P^+ = 60$ MPa), $\alpha_d = 9.1 \times 10^5\ s^{-1}$ is the decay constant, $\omega = 2\pi f$ is the radial frequency with $f = 83.3$ kHz, $C_o = 3$ is constant and t is time [48]. This shock is characterized by 1 µs compressive and 5 µs tensile waves. The shock pressure of 60 MPa is rather high compared with the level that is likely to be generated in tissue [49]. However, it is the level that is typically generated during laboratory experiments (e.g. 65 MPa shock pressure in [20] and 10–100 MPa shock pressure in [12]), which could be used to validate the prediction of this paper (in which bubble dynamics are observed by high-speed photography in water and pressure pulses measured by hydrophones placed in it, which is not possible in humans *in vivo*) and where lithotripter shocks are sent through water baths.

Three cases were simulated based on the dimensionless distance $\xi = d/R_0$ (i.e. 0.75, 0.875, 0.95), where $R_0 = 40$ µm and d is the separation distance between the bubble's centre and the wall. The water and the air bubble were assumed to be initially in equilibrium and under standard atmospheric conditions ($p_w = p_a = 101.325$ kPa, $\rho_w = 1000\ kg\,m^{-3}$, $\rho_a = 1.2246\ kg\,m^{-3}$ and $T_w = T_a = 288.15$ K). The subscripts 'w' and 'a' refer to the water and air bubble, respectively. The surface tension of the fluids was neglected. The evolution of the bubble is shown in figure 2. As many bubble jetting simulations have shown, the bubble's upstream surface accelerates towards the wall to form a jet that pierces the bubble so it forms a toroid (figure 2*d*(i)). Prior to Turangan *et al.* [3], previous simulations [23,27,50] had to cease before the moment the jet impacts the bubble's downstream wall, but FLM [3,4,21] showed that this impact produces an intense blast wave containing pressures that are two to three orders of magnitude greater than the original incident shock.

Key features are labelled as follows. Referring to figure 2, initially, the lithotripter shock MS (initiated at a distance of 120 µm from the bubble's centre) impacts the bubble surface and transmits a weak shock TS into the bubble and a strong expansion wave EW into the surrounding water. Over time, the pressure gradient in the water in the vicinity of the bubble's upstream surface increases. This surface eventually forms a high-speed axial jet that moves along the symmetry axis. Inside the bubble, a bow shock SS is created in front of this accelerating jet. Here, the content of the attached bubbles is in direct contact with the solid. Such cases are fundamentally different from the detached bubble scenarios ($\xi > 1$). This is because the impact of the bow shock SS and the jet on the wall is direct as there is no water layer separating the bubble from the wall, which may affect the surface erosion [49]. The jet impact emits a very strong asymmetric blast wave into the surrounding water, which subsequently interacts with the isolated toroidal bubble,

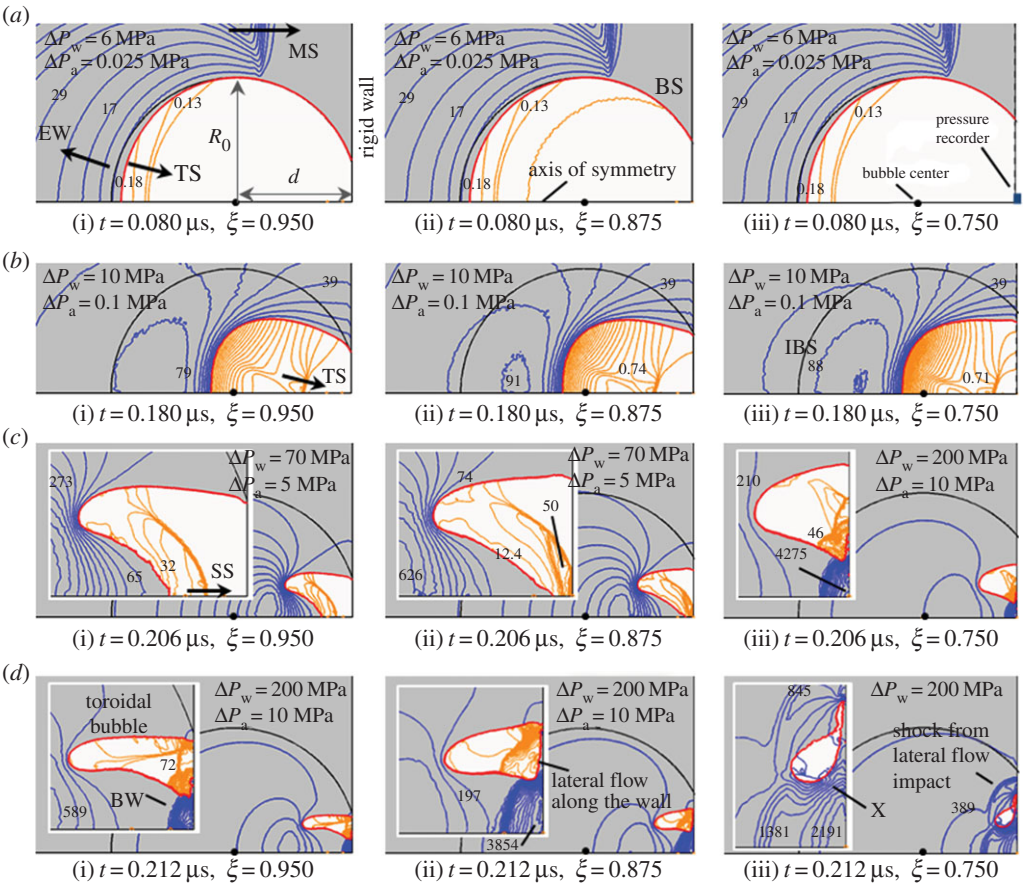

Figure 2. The plots of pressure contours showing the interaction of the bubble with the lithotripter shock for three different distances $\xi = d/R_0$. The bubble elongates because of the additional compression by the shock reflection. Label MS denotes the lithotripter main shock, EW is the expansion wave and TS is the transmitted shock. Their directions are indicated by arrows. IBS is the initial bubble surface and BS is the current bubble surface. The bow shock SS is formed inside the bubble in front of the accelerating jet. The jet impacts the wall with a velocity greater than 2 km s^{-1}, generating a blast wave BW and a lateral jet sheet (splash) along the wall. Inset is the close-up view of the event. (Online version in colour.)

causing it to collapse further (e.g. in figure 2*d*(ii),(iii)). Prior to jet impact, the bow shock SS forms an oblique reflection inside the bubble (figure 2*c*(ii),(iii)). As the wall is not allowed to deform, the jet is redirected in the lateral direction. It consequently forms a radially spreading water splash that propagates out along the wall (figure 2*d*(ii),(iii)), similar to the features of a high-speed liquid impact on solids [51], e.g. droplet impact on high-speed moving objects.

The high-speed jet velocity time histories of these attached bubble cases are plotted in figure 3*a* together with some of the detached bubbles (e.g. presented in [4]) and a free-field bubble for comparison. The plots indicate that the bubble's upstream surface velocity initially increases in a gradual fashion but then accelerates to form the jet as the bubble contracts. The curves are almost identical up to $t \approx 0.15\,\mu$s from the initiation but then vary after the reflection of the incident shock as the wall engulfs the bubble. Apart from $\xi = 2.0$ and $\xi = \infty$ (free field), whose jet velocity only reaches less than 1.4 km s^{-1}, the other cases have jet velocities that exceed 2 km s^{-1}.

The time histories of the pressure loading on the wall (figure 2*a*(iii)) for different distances ξ plotted in figure 3*b* show that in general, for detached bubbles ($\xi > 1$), the peak pressure decreases significantly as ξ increases. A pressure of about 6.7 GPa is recorded when $\xi = 1.0625$. It then drops to 2.5 GPa when $\xi = 1.25$ and to 0.5 GPa when $\xi = 2.0$. For attached bubbles with

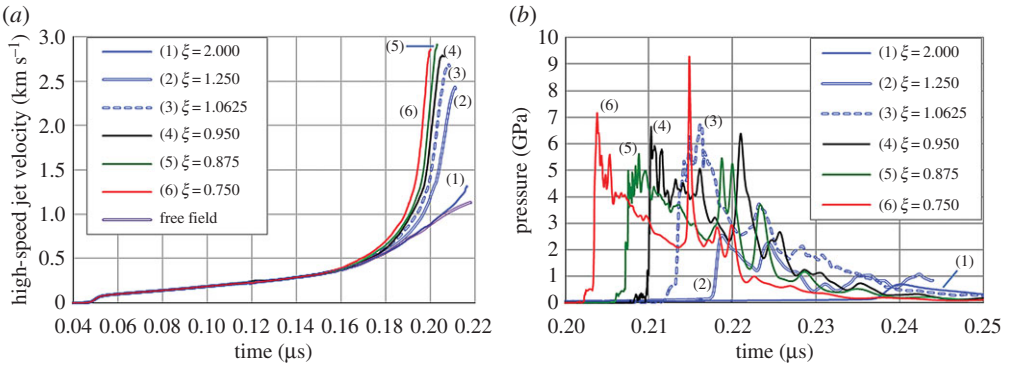

Figure 3. (*a*) The velocity time histories of the high-speed axial jet of the bubble. (*b*) The pressure loading time histories recorded on the rigid wall along the symmetry axis (figure 2*b*(ii)) are generally characterized by two major peaks: the first represents the blast wave emission from the jet impact, and the second is associated with the pressure wave implosion at the symmetry axis. The 60 MPa lithotripter shock is initiated at a distance of 120 μm from the bubble's centre (figure 4). (Online version in colour.)

$\xi = \{0.95, 0.875, 0.75\}$, the pressure loadings on the wall are of a similar order of magnitude (between 5 and 9 GPa). Their pressure time histories are characterized by two major peaks that are separated by a 0.01 μs duration. The first peak represents the blast wave emitted when the jet impacts the wall, and the second peak is associated with the pressure wave implosion at the symmetry axis. This high-pressure wave, which strengthens as it moves radially inwards along the wall towards the symmetry axis (labelled 'X' in figure 2*d*(iii)), is found to originate from the complex reflection of the blast wave by the toroidal bubble and the rigid wall. For $\xi = 0.75$, the pressure can reach as high as 9 GPa. Another slightly weaker pressure peak recorded after the second major peak is associated with the rebound of the toroidal bubble.

(b) Single bubbles near and attached to an aluminium wall

When the bubble is attached to an elastic–plastic solid, the collapse dynamics are different from those with a rigid wall because the structural changes to the solid caused by the jet impingement affect the local flow field. Here, aluminium is used as the elastic–plastic solid with properties: $\rho_{al} = 2785\,\mathrm{kg\,m^{-3}}$, shear modulus $\mu_{al} = 26.5$ GPa and yield strength $Y_0 = 0.3$ GPa. As illustrated in figure 4, a 60 MPa peak pressure lithotripter shock (equation (3.1)) propagates towards the bubble. The radius $R_0 = 40\,\mu\mathrm{m}$ of the fully spherical bubble is used as a scaling parameter. At $t = 0$, the shock is generated at a distance $L_s = 120\,\mu\mathrm{m}$ from the bubble's centre. Twelve generic cases were simulated, i.e. $\xi = d/R_0 = \{2.0, 1.5, 1.25, 1.125\}$ for a detached bubble and $\xi = \{0.95, 0.875, 0.75, 0.5, 0.25, 0, -0.25, -0.5\}$ for an attached bubble. The simulation time starts from when the shock is initiated at $L_s = 120\,\mu\mathrm{m}$. A non-dimensional interface smoothing gain α associated with the restoring force for the artificial surface tension was determined by trial and error from some preliminary simulations with different values tested (i.e. $\alpha = 10, 100, 1000$). This depends on how fine the mesh around the air–water interface is. The gain $\alpha = 100$ that corresponds to a maximum correction of about 0.01% to the interface particle displacement for every time step was optimum, whereas $\alpha = 10$ was so low that interface wrinkles were still apparent, and $\alpha = 1000$ was so high that it produced a slightly earlier collapse.

(i) Free field versus rigid wall versus elastic–plastic wall (aluminium)

We first compare the bubble's morphological changes and the surrounding flow field of the case of a bubble attached to an elastic–plastic solid ($\xi = 0.95$) with the cases of a bubble in a free field and that is attached to a rigid wall. For the aluminium wall case, the domain is initially

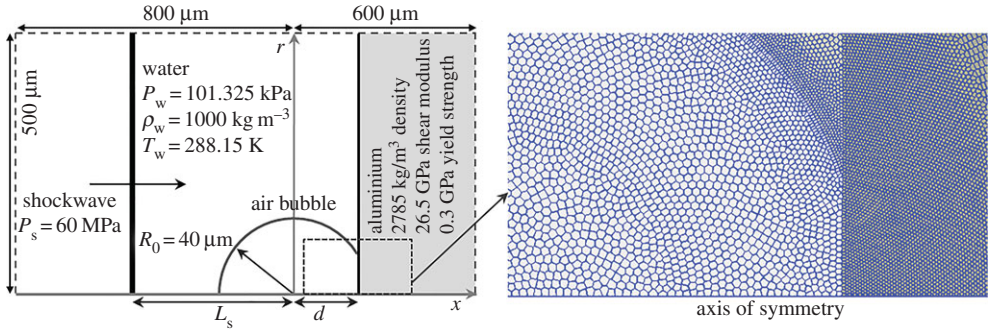

Figure 4. The computational domain of a bubble attached to aluminium (bubble centre's non-dimensional distance from the aluminium $\xi = d/R_0$), and a close-up view of the Voronoi mesh around the attachment region. L_s is the distance of the lithotripter shock from the bubble's centre at $t = 0$. Apart from the axis of symmetry (solid boundary), non-reflecting inflow/outflow boundary conditions are applicable to the other domain boundaries. The fluids and solid are initially at standard atmospheric conditions. The artificial surface tension [35] that helps to suppress the amplitude and growth rate of the small-scale perturbation of mesh-induced wavenumber instabilities on material interfaces is applied to air–water interfaces only because, for solid materials, interface deformation is not influenced by these mesh-induced errors [36]. (Online version in colour.)

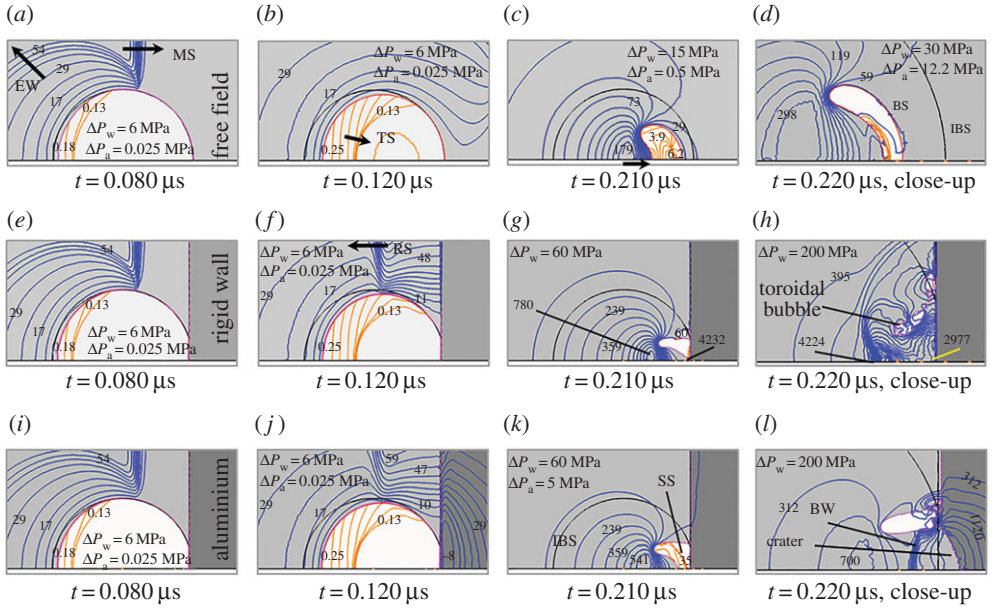

Figure 5. A comparison of the shock-induced collapse of a single bubble in a free field and that attached to a rigid and aluminium wall showing the plots of pressure contours at different times. The shock MS is reflected back in the water as a shock RS by the walls, and is also partially transmitted into the aluminium. The bubble's upstream surface forms a high-speed jet that accelerates towards the wall, and on impact it generates a blast wave BW. The transmitted shock in the bubble TS, initial bubble surface IBS, current bubble surface BS and bow shock SS in the bubble are labelled accordingly. The directions of the waves and high-speed jet are shown. The pressure contour unit is in megapascal. (Online version in colour.)

discretized using 49 293 computational cells (4920 for the air bubble, 33 055 for the water and 11 318 for the aluminium), for a bubble in the free-field case using 45 764 cells (5056 for the air bubble and 40 708 for the water) and for the rigid wall case using 37 975 cells (4920 for the air bubble and 33 055 for the water). These computational cells are deemed to be sufficient to capture the physics of the shock-induced bubble collapse, as shown in our previous work [4]. The

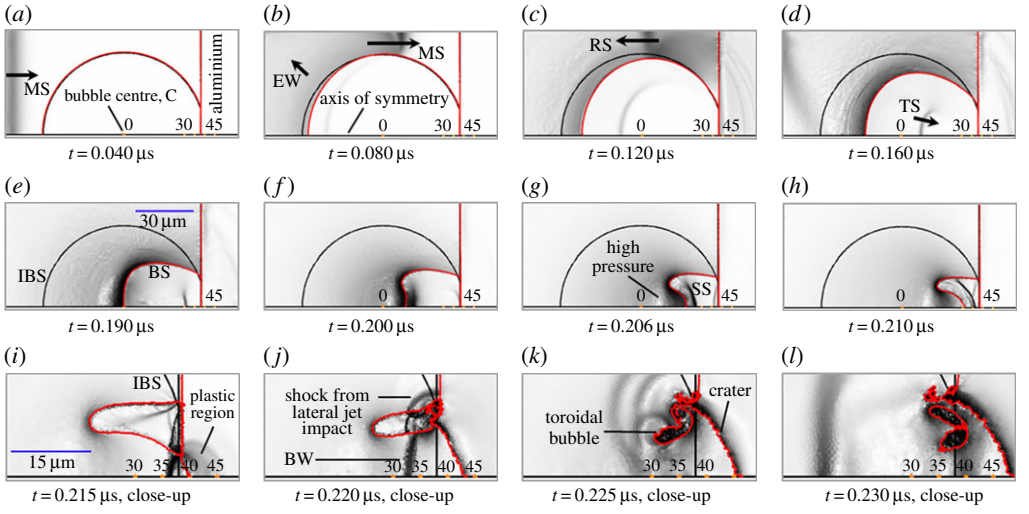

Figure 6. Schlieren-like (density gradient) plots of bubble evolution after its interaction with a 60 MPa lithotripter shock MS ($R_0 = 40\ \mu$m, $\xi = 0.95$). The incorporation of the compressibility, multi-phases, axisymmetric geometry and elastic–plastic material model within a single solver has enabled us to examine the impingement of high-speed liquid jets that impose an extreme compression in the aluminium, which forms a crater and produces plastic deformation. (Online version in colour.)

simulation time step is controlled by the Courant–Friedrichs–Lewy (CFL) number and CFL ≤ 0.4 has been used.

At $t = 0.08\ \mu$s (in figure 5), the flow patterns are similar in all three cases. At $t = 0.12\ \mu$s, the lithotripter shock MS has traversed the bubble in a free field, it has been fully reflected by the rigid wall and has been partially reflected by the aluminium. The full reflection of the shock MS by the rigid wall results in a slightly stronger reflected shock RS than the weaker reflection when the wall is aluminium. Consequently, the region behind the reflected shock RS (between the wall and the bubble's surface) has a slightly higher pressure than that with the aluminium. In the rigid and aluminium wall cases, the reflected shock RS further compresses the collapsing bubble but the effects are more profound for the case with a rigid wall, causing the collapse to be faster as indicated by an early high-speed jet impact seen at $t = 0.21\ \mu$s (figure 5*g*). The jet impacts the wall directly, emitting an intense blast wave and turning the bubble into a toroid. At $t = 0.22\ \mu$s, while the high-speed jet is yet to impact onto the opposite side of the bubble in a free field (figure 5*d*), the jet has already pierced the bubble attached to the rigid wall and induced a lateral motion for the now-toroidal bubble that is seen sliding outwards along the wall (figure 5*h*). However, for the aluminium wall case, the jet impingement produces a crater (and plastic deformation) in which the toroidal bubble is being drawn into a vortex ring (figure 5*l*).

(ii) The collapse of a bubble with $\xi = 0.95$

The evolution of a bubble with $\xi = 0.95$ is shown in figures 6 and 7. From the shock initiation until the bubble is drawn into the crater, the duration is about 0.24 µs. This is less than the compressive wave duration of the lithotripter shock MS of 1 µs, which means that the events are confined within the compressive wave period. When the shock MS with 60 MPa peak pressure impacts the aluminium, it does not cause any plastic deformation because the pressure is significantly less than the 0.3 GPa yield strength of the aluminium model. Instead, the transmitted shock in the aluminium manifests into an elastic or longitudinal wave that propagates with a velocity $c = \sqrt{E_{\mathrm{al}}/\rho_{\mathrm{al}}}$ (where E_{al} and ρ_{al} are Young's modulus and the density of aluminium, respectively). The presence of the bubble that blocks the shock MS imposes a tension (negative pressure) in the aluminium around the contact surface, as shown in figure 5*j*.

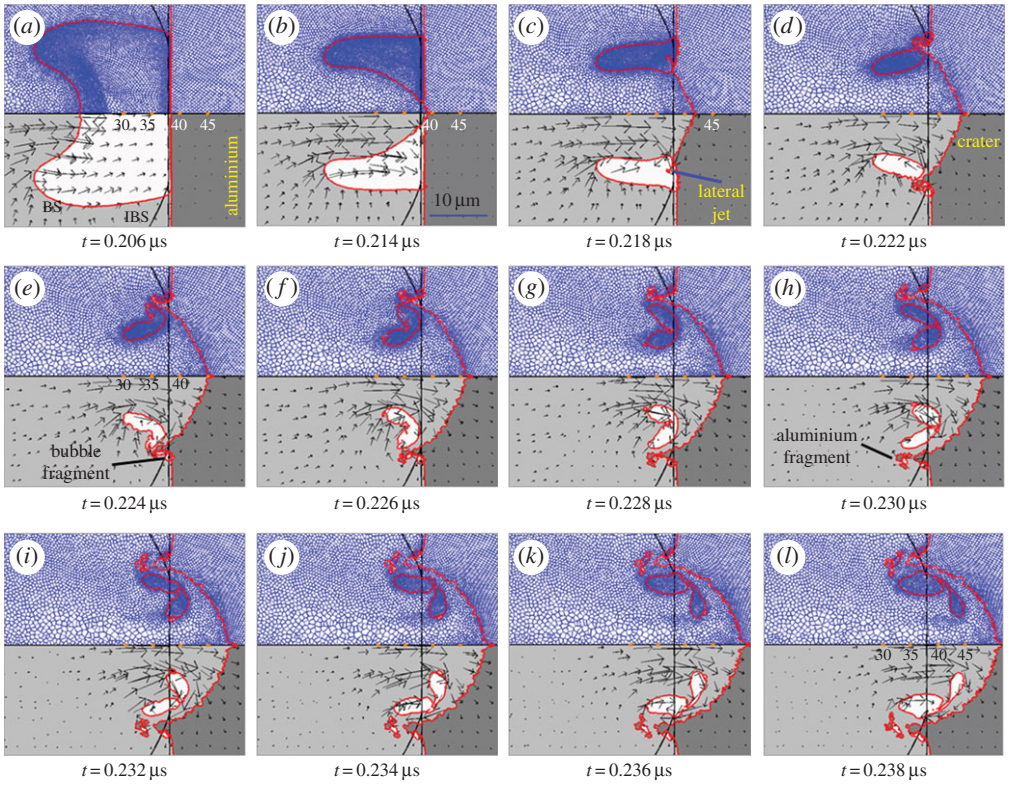

Figure 7. The plots of a Voronoi mesh and velocity vectors of the bubble after the high-speed jet has fully formed. It shows how the jet impact occurs and the bubble turns into a toroidal shape. The jet impact forms an oblique lateral jet sheet that propagates away from the symmetry axis, which helps to split the bubble section that is attached to the aluminium. The jet impingement creates a crater and squeezes out some aluminium fragments. The bubble is then drawn into the crater by the vortex ring. The vertical solid line represents the original surface of the aluminium at $t = 0$. (Online version in colour.)

After impacting the aluminium, the incident shock MS is partially reflected back into the water as a shockwave RS. When the reflected shock RS hits the bubble's surface near the contact line, it is also partially reflected back as an expansion wave (figure 6*c*), and thus lowers the pressure in this region. This appears to keep the contact line of the bubble on the aluminium unchanged. The propagation of reflected shock RS on the bubble's surface imposes a shear that not only squeezes the bubble further but also tends to elongate it. When the bubble contracts, the transmitted shock TS inside the bubble strengthens as a result of a focusing effect induced by the contracting bubble surface. At $t = 0.16\,\mu$s, the bubble is now fully submerged in a high-pressure field behind the reflected shock RS. The bubble's upstream surface then accelerates downstream.

At $t = 0.20\,\mu$s, the bubble's upstream surface has flattened, and the bow shock SS starts to form inside the bubble in front of the jet. At $t = 0.21\,\mu$s, the bow shock arrives at the aluminium surface and intersects with the transmitted shock TS that has just been reflected back by the wall. The jet impacts the aluminium with a $2.16\,\mathrm{km\,s^{-1}}$ velocity, i.e. 23% lower than the $2.8\,\mathrm{km\,s^{-1}}$ velocity when the wall is rigid (figure 3). This supersonic jet impact on the wall emits a blast wave BW that further contracts the now-toroidal bubble at $t = 0.22\,\mu$s. Multiple waves are seen at $t = 0.225\,\mu$s, but they eventually merge into one. The vortex ring surrounding the toroidal bubble draws the bubble into the crater formed by the jet impingement. The crater area is the same as the bubble's contact surface, and the crater depth is approximately $13.7\,\mu$m (i.e. 34.3% of the bubble radius R_0).

The change in the bubble's shape and surrounding flow field during the final stage of the collapse is shown in figure 7. The computational mesh evolves as it mimics the flow. Inside the

bubble, a dense mesh is formed in front of the accelerating jet, which represents a compressed region in the bubble. Instead of redirecting the jet along the aluminium surface (as in the rigid wall case), the lateral jet sheet (splash) from the impact is directed in an oblique fashion (at $t = 0.218\,\mu s$) because the aluminium deforms. This jet sheet eventually splits out a small fraction of the bubble adjacent to the aluminium (see the frame sequence of figure 7*c–f*).

For the aluminium (modelled using the elastic–perfectly plastic model), the morphological changes are strictly subjected to satisfying the yield condition given by equation (2.11). Here, the impact of a $2.16\,km\,s^{-1}$ jet imposes an extreme compression in the aluminium that, under this circumstance, starts to behave like a fluid, whereby a permanent deformation in the form of a crater is produced. From $t = 0.222\,\mu s$ onwards, when the jet continues to penetrate, the aluminium cells are squeezed out around the tip of the jet. This occurs to such an extent that these cells are stretched to the point whereby tensile forces cannot be transferred to them. At this stage, the aluminium material fails and undergoes a 'numerical fragmentation' and the cells become separated from the main bulk of aluminium as they are ejected. This exhibits patterns similar to those observed in the high-velocity projectile impacts by Howell & Ball [36]. The damage associated with this shock-induced collapse is more profound than the one caused by the inertial collapse (an underwater explosion type), e.g. in the simulation by Chahine & Hsiao [33], primarily because of the vast difference in the jet velocity between these two types of collapse.

The use of a Voronoi mesh that convects with the local flow velocity results in a dynamic change of the mesh topology that requires frequent re-meshing to prevent mesh distortion. How smooth the material interfaces are (defined by the boundaries shared between dissimilar materials) is determined by the mesh resolution around them. The aluminium crater formed after the jet impact (figures 6*i–l* and 7*c–l*), when looked at closely, is not very smooth, which is inherent to the use of finite numbers of computational cells. Generally, the characteristics of the fluid phenomena observed agree with the experimental evidence [52,53] and are a high-pressure analogy of the response of bubbles to pressure gradients that are observed at lower amplitudes. Such behaviour has practical implications when multiple shocks are projected at a solid and may cause crack propagation and the fragmentation of solids, which might be desirable (as in lithotripsy [9]) or undesirable (as in pulsed neutron sources [39]). With sufficient computational resources, for example, this approach would allow investigation of the role in erosion of the survival of bubble nuclei between shocks and the nucleation of cavitation by subsequent (lithotripter [9]) shocks.

(iii) Comparison of the collapse patterns for different distances ξ

The response of the bubble following its interaction with the lithotripter shock MS is examined for 12 case studies, i.e. $\xi = \{2.0, 1.5, 1.25, 1.125, 0.95, 0.875, 0.75, 0.5, 0.25, 0, -0.25, -0.5\}$, that have been designed to represent both the attached ($\xi \leq 1$) and detached bubbles ($\xi > 1$), with the aim of evaluating how the distance ξ affects the collapse patterns. Negative values of distance ξ represent the bubbles whose size is less than half of their fully spherical size. Owing to the relative distance of the aluminium surface from the bubble's centre, the interaction varies from case to case.

As depicted in figure 8 at $t = 0.12\,\mu s$, for the detached bubbles, i.e. $\xi = \{2.0, 1.5, 1.25, 1.125\}$, the interaction of the weak-reflected shock and the right side of the bubble creates a low-pressure region in the water that separates the bubble from the aluminium. This drop in pressure also occurs for the cases of attached bubbles ($\xi = \{0.95, 0.875, 0.75, 0.5\}$), resulting in a nearly unchanged contact line of the bubble on the aluminium. As ξ reduces further ($\xi = \{0.25, 0, -0.25, -0.5\}$), this pressure drop vanishes. The stagnation region behind the reflected shock RS (with pressure nearly double that of the shock MS) causes the contact line of the bubble to move radially inwards. For $\xi = \{0, -0.25, -0.5\}$, this leads to the 'pinching' of the bubble as its surface near the contact line accelerates to form the inward jet flow (figure 8*l*).

Referring to figure 9, the collapse features and damage patterns can be grouped into: (i) detached bubbles with $\xi > 1$, (ii) attached bubble with $0 < \xi \leq 1$, and (iii) attached bubble with $\xi \leq 0$. The depth of the craters is plotted in figure 10*b*. For $\xi = 2.0$, there is no noticeable

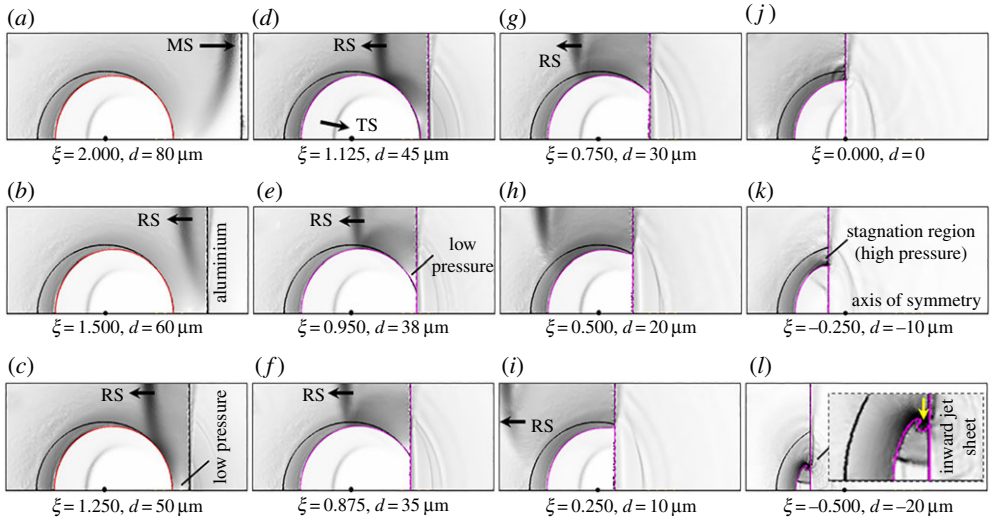

Figure 8. Schlieren-like plots of the interaction of the lithotripter shock MS with the bubble at $t = 0.12$ μs show the features of shock interaction with the bubble and the wall, and the subsequent bubble's evolution for detached bubbles with $\xi = \{2.0, 1.5, 1.25, 1.125\}$ and attached bubbles with $\xi = \{0.95, 0.875, 0.75, 0.5, 0.25, 0, -0.25, -0.5\}$. (Online version in colour.)

depression in the aluminium as the considerably thicker water layer (which separates the bubble from the aluminium) helps to prevent the jet from impinging on and damaging the aluminium even though the blast wave BW from the jet impact is still able to strike the aluminium. For $\xi = 1.5$, there is only a minimal depression in the aluminium, which is caused primarily by the blast wave BW. It is similar for $\xi = 1.25$, but the depression is more obvious. For $\xi = 1.125$, however, the depression is significant as it is produced by both the blast wave and the jet impact.

For the attached bubbles with $\xi = \{0.95, 0.875, 0.75, 0.5\}$, the structural damage to the aluminium is fundamentally different from that of detached bubbles. Here, the damage exhibits characteristics similar to those of high-speed projectile impacts [36]. The aluminium subjected to the impingement of liquid jets moving at very high velocities (greater than 2 km s^{-1}) behaves like a fluid. The impact produces a crater, from which some aluminium fragments are squeezed out from the surface. The redirection of the jet upon impact onto the aluminium, which results in the formation of an oblique jet sheet, is also evident. The bubble with $\xi = 0.25$, however, produces a crater similar to the one with $\xi = 1.125$. However, for $\xi = 0.25$, apart from the high-speed axial jet, an inward-moving radial flow along the aluminium surface is also formed.

For the attached bubbles with $\xi \leq 0$ (e.g. 0, −0.25, −0.50), the collapse is characterized by the absence of the high-speed axial jet and the presence of the inward-moving radial flow along the aluminium. The pinching of the bubbles by this radial flow, whose velocity, for example, for $\xi = -0.25$ can be as high as 1.8 km s^{-1}, forms mushroom-like shapes (figure 9*j*,*k*,*l*). As the pinching strengthens, the bubbles undergo an extreme compression. The pressure in the bubbles can be extremely high as the radial flow approaches the horizontal axis. However, our simulations with $\xi \leq 0$ were not continued beyond the times given in figure 9*j*,*k*,*l* because of the precaution imposed on the use of the ideal gas EOS associated with this extreme pressure. Up to these times, therefore, no evidence of plastic deformation (crater) is observed except for a very minimal depression in the aluminium when $\xi = 0$ and −0.25. Lauer *et al.* [47] predicted the transformation from a mushroom to a 'pin'-shaped bubble (that later detaches from the wall) when the pinching continues by assuming that the bubble contains only vapour and the collapse is initiated by a higher uniform liquid pressure surrounding the bubble (Rayleigh collapse), i.e. two fundamental differences as compared with our scenarios of air-contained bubbles and the collapse is induced by a shockwave.

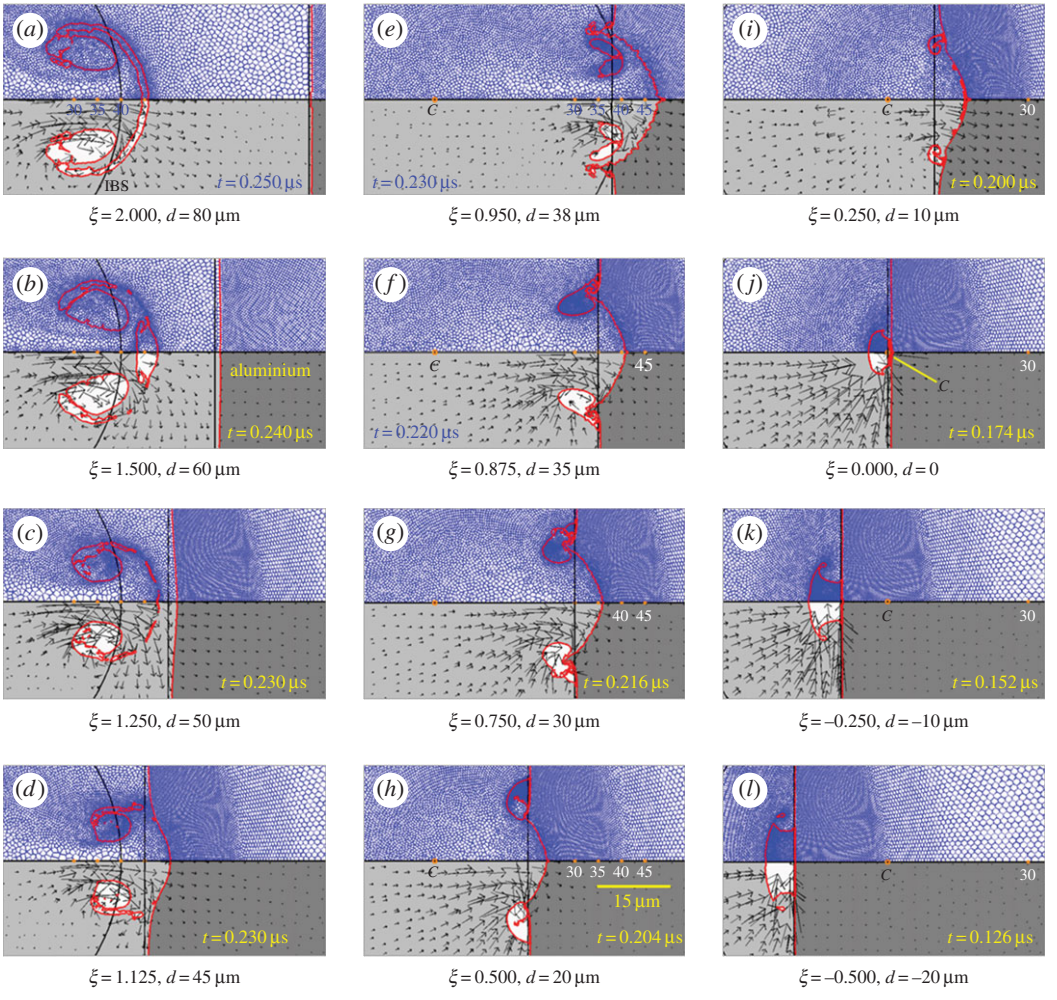

Figure 9. Plots of a Voronoi mesh and velocity vectors showing how the mesh evolves with the flow for different ξ. These plots (given at different times) show the response of the aluminium as an elastic–plastic solid to the jetting collapse of the bubble, and the possible structural damage of the aluminium. The severe damage is associated with a direct or near direct impact of the axial jet from the collapsing bubbles residing very close to or attached to the aluminium, i.e. with $\xi = \{1.125, 0.95, 0.875, 0.75, 0.5, 0.25\}$. (Online version in colour.)

As shown in figure 10*a*, for $\xi > 0$, the maximum jet velocity increases to reach a peak of about 2.31 km s^{-1} and gradually reduces to approach the 1.14 km s^{-1} mark of a free-field bubble ($\xi = \infty$). For $\xi \leq 0$, although the bubble's upstream surface accelerates to a velocity of nearly 0.4 km s^{-1} or above, it does not transform into an axial high-speed jet because of the nature of how these bubbles are attached to the wall and how they contract in response to the incident shock MS. The maximum depths of the crater can reach greater than 13 µm, i.e. for $\xi = \{0.95, 0.875, 0.75\}$ (figure 10*b*). For higher distances ξ, the depth reduces tremendously. The crater depth and size appear to correlate well with the speed of the axial jet and whether the impact is direct or indirect. Referring to figure 9, two types of crater are identified: (i) craters with a gradual and smooth edge, which are produced by either an indirect jet impact (e.g. with $\xi > 1$) or a direct jet impact coupled with an inward radial flow (e.g. with $\xi = 0.25$), and (ii) craters with a sharp and well-defined edge, which are produced almost solely by a direct jet impact (e.g. with $\xi = \{0.95, 0.875, 0.75, 0.5\}$).

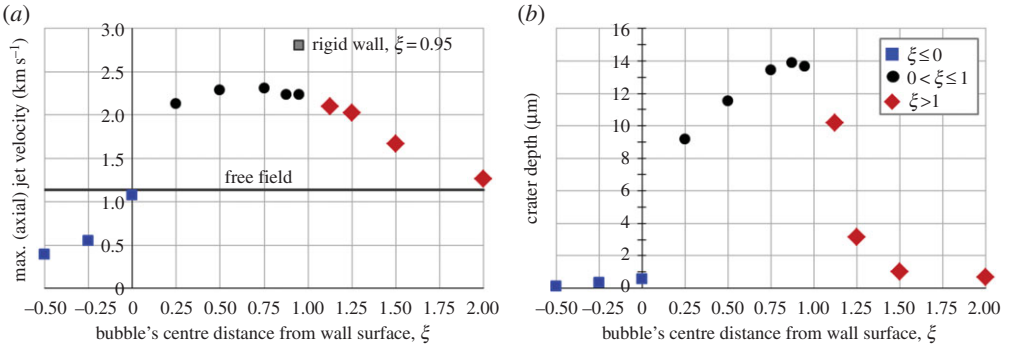

Figure 10. (*a*) The plot of maximum axial jet velocity (bubble's upstream surface) for different distances ξ. The cases for a bubble in the free field (1.14 km s^{-1}) and attached to a rigid wall with $\xi = 0.95$ (2.8 km s^{-1}) are included for comparison. For $\xi = \{0, -0.25, -0.50\}$, the axial jet is not materialized. (*b*) The plot of crater depths for different distances ξ. (Online version in colour.)

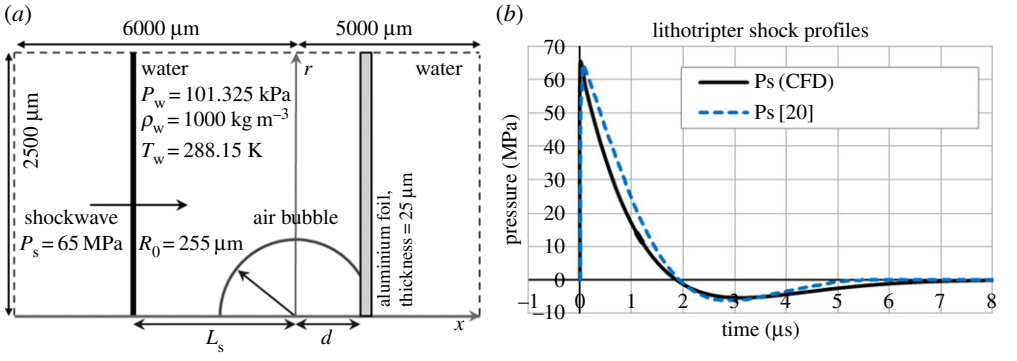

Figure 11. (*a*) The domain for the simulation of a lithotripter shock-induced collapse of a 255 μm radius bubble attached to a 25 μm thick aluminium foil for qualitative comparison with the experiment of Philipp *et al.* [20]. The aluminium foil model has 2785 kg m^{-3} density, 26.5 GPa shear modulus and 0.3 GPa yield strength. $d = 242.25$ μm and the bubble's centre distance is $\xi = d/R_0 = 0.95$. The shock is generated at a distance $L_s = 500$ μm from the bubble's centre. (*b*) The lithotripter shockwave profiles used in the simulation and in the experiment. (Online version in colour.)

(c) Comparison with experiment for a bubble attached to aluminium foil

In the experiment by Philipp *et al.* [20], single bubbles (150 μm–1.2 mm radius) were collapsed by a lithotripter shock. The shock peak pressure was about 65 MPa, and was generated using electrodes with a focusing ellipsoid (XL 1; Dornier Medizintechnik). The idealized pressure profile of the shock is shown in figure 11*b*. The bubbles were attached to a 25 μm thickness acrylate-coated polypropylene material that has an area density of 22.7 g m^{-2} and a tensile strength between 155 and 250 N mm^{-2}. In our simulation, because of resource limitations only the case of an $R_0 = 255$ μm radius bubble is simulated. As the acrylate-coated polypropylene material model is not available in the present scheme material database, aluminium is used instead to represent the elastic–plastic solid foil to which the bubble is attached. The schematic of the computational domain is shown in figure 11*a*. The equation for the idealized lithotripter shock pressure profile used in the experiment was not given; therefore, the shock profile used in the simulation was approximated using equation (3.1), i.e. with values $P^+ = 40$ MPa, $\alpha_d = 7 \times 10^5$ s^{-1}, $f = 80$ kHz and $C_o = 5$. This shock reaches a pressure peak of $P_s \approx 65$ MPa. Initially, 46 918 computational cells are used, i.e. 4920 for the air bubble, 39 461 for the water and 2537 for the foil.

The simulation presented in figure 12 shows the evolution of the Voronoi mesh that mimics the flow, the Schlieren-like (density gradient) that captures the shock propagation in the early

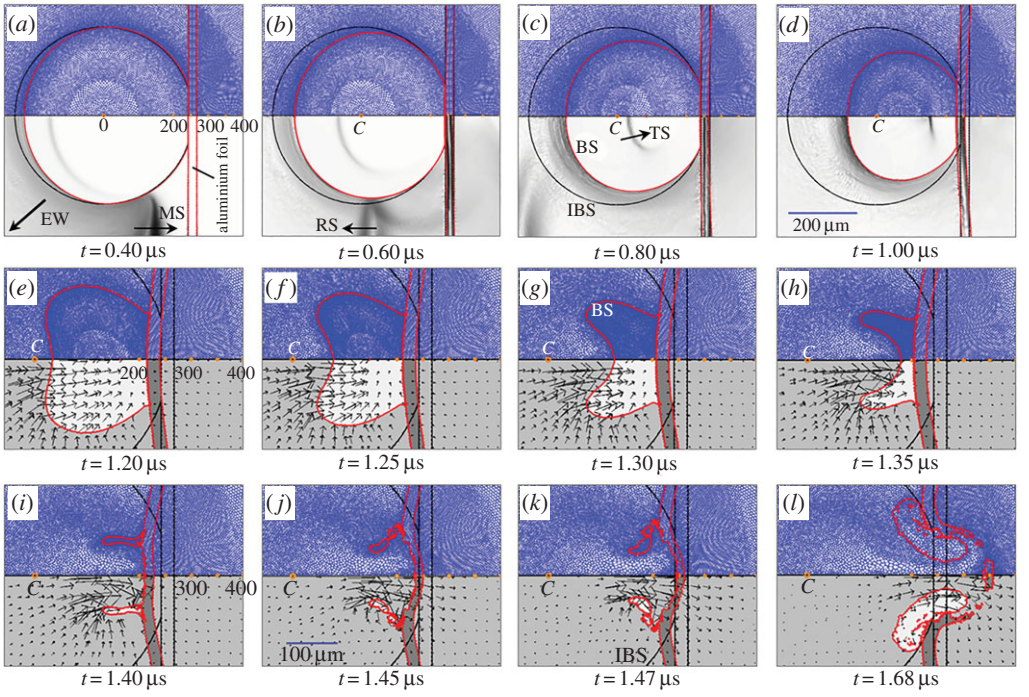

Figure 12. The plots of a Voronoi mesh (top half) with Schlieren-like ((*a–d*) bottom half) and a Voronoi mesh with velocity vectors ((*e–l*) bottom half) that show the interaction of the lithotripter shockwave with a single bubble attached to aluminium foil. The foil tends to sway together with the flow but is eventually pierced by the high-speed jet from the collapsing bubble. (Online version in colour.)

stage of the interaction and the velocity vectors that indicate the flow direction at different times. The beginning of the interaction has similar features to the earlier simulations (including the expansion wave EW and transmitted shock TS). However, when the shock MS hits the aluminium foil, it is reflected as a shock and a rarefaction (seen as a two-wave structure in figure 12*b*) because the foil has a finite thickness. The contraction of the bubble causes a suction that sways the aluminium foil towards the centre of the bubble. The bubble's upstream surface eventually accelerates to form the high-speed jet. At $t = 1.35\,\mu s$, the aluminium foil is seen to have moved to the 200 µm mark on the symmetry axis. The high-speed axial jet with velocity reaching $1.05\,km\,s^{-1}$ impacts the foil at $t \approx 1.37\,\mu s$ after the initiation. As shown in figure 12*i*, at $t = 1.40\,\mu s$, the now-toroidal bubble shape is relatively thinner than that of the 40 µm bubble attached to an aluminium wall. The impact of the jet pushes the foil downstream again, and the flow produces a vortex ring after the jet impact. The aluminium foil tends to stretch only, without being penetrated by the jet at least until $t = 1.47\,\mu s$. However, the foil is eventually pierced, which appears to be caused by both the flow behind the jet and the expansion of the toroidal bubble (figure 12*l*). Some aluminium fragments are carried downstream by the flow.

The maximum jet velocity of $1.05\,km\,s^{-1}$ is substantially lower than the $2.16\,km\,s^{-1}$ of that with a 40 µm radius bubble. This may be due to factors such as the relative size of the bubble with respect to the lithotripter shock peak pressures and the type of boundary being used, i.e. aluminium foil instead of an aluminium wall. When compared with the experiment by Philipp *et al.* [20], both the experiment and simulation show that the foil is pierced by the collapse of the bubble. Although the size of the hole is similar, i.e. ≈150 µm, the patterns are quite different. In the experiment, it looks as though the foil was torn, which may be typical of materials made of plastics. In the simulation, the aluminium foil is seen to be fragmented by the flow. For decades, the pitting of aluminium foil has been the preferred method by which industry has found a proxy for the cleaning performance of an ultrasonic cleaning bath [54]. While 'cavitation jets' have

been the accepted explanation for the formation of punctures in the foil, this is the first simulation of the process that allows prediction of the magnitudes of the forces at play, the material responses and the details of the mechanism.

4. Conclusion

The FLM that incorporates compressibility, multi-phases and elastic–plastic solid models has been used to simulate the collapse of 40 µm radius single bubbles attached to/near rigid and aluminium walls by a 60 MPa lithotripter shock, and the collapse of a 255 µm radius bubble attached to 25 µm thick aluminium foil by a 65 MPa lithotripter shock. The collapse events of the bubble attached to the aluminium are different from those with a rigid wall because the aluminium is allowed to deform after the jet and the blast wave impingement. The study of the collapse for different distances ξ from the aluminium ($\xi > 1$, $0 < \xi \leq 1$ and $\xi \leq 0$) shows different characteristics in the collapse dynamics (i.e. bubble jetting or bubble pinching) and different damage/crater patterns (i.e. gradual and smooth edge or sharp and well-defined edge with material ejection). The results strongly indicate that the deformation in solids subjected to cavitation and shock interaction is primarily associated with the direct or near direct impact of the axial jet from collapsing bubbles attached to or residing very close to the solids (i.e. $0 < \xi < 1.25$), and the blast wave impact appears to be only the secondary cause. The damage patterns, e.g. for $\xi = \{0.95, 0.875, 0.75, 0.5\}$, exhibit characteristics similar to those of the high-speed projectile impact. Qualitative comparison with the experiment for the 255 µm radius bubble attached to 25 µm thick foil shows that the bubble jetting collapse pierces the foil with a similar sized hole but with a different hole pattern owing to the different material properties of the foils. With the use of the elastic–perfectly plastic material model, we are able to model the response of the solid under extreme loading in the context of shock-induced bubble collapse. An improvement in the constitutive models, e.g. with the use of the Johnson & Cook model [55], may further enhance the applicability of the current scheme to model the yield of solid materials more accurately.

Data accessibility. This work does not have any experimental data. The data supporting this study are openly available from the University of Southampton repository at https://doi.org/10.5258/SOTON/D0195 [56].

Authors' contributions. All authors contributed equally and gave final approval for publication.

Competing interests. We have no competing interests.

Funding. A.R.J. was supported through a PhD studentship provided by the EPSRC (grant no. GR/N19243; principal investigator: T.G.L.).

References

1. Bourne NK, Field JE. 1999 Shock-induced collapse and luminescence by cavities. *Phil. Trans. R. Soc. Lond. A* **357**, 295–311. (doi:10.1098/rsta.1999.0328)
2. Ball GJ, Howell BP, Leighton TG, Schofield MJ. 2000 Shock-induced collapse of a cylindrical air cavity in water: a free-Lagrange simulation. *Shock Waves* **10**, 265–276. (doi:10.1007/s001930000060)
3. Turangan CK, Jamaluddin AR, Ball GJ, Leighton TG. 2008 Free-Lagrange simulations of the expansion and jetting collapse of air bubbles in water. *J. Fluid Mech.* **598**, 1–25. (doi:10.1017/S0022112007009317)
4. Jamaluddin AR, Ball GJ, Turangan CK, Leighton TG. 2011 The collapse of single bubbles: an approximation of the far field acoustic emissions for cavitation induced by shock wave lithotripsy. *J. Fluid Mech.* **677**, 305–341. (doi:10.1017/jfm.2011.85)
5. Hawker NA, Ventikos Y. 2012 Interaction of a strong shockwave with a gas bubble in a liquid medium: a numerical study. *J. Fluid Mech.* **132**, 1–39. (doi:10.1017/jfm.2012.132)
6. Zhang S, Duncan J, Chahine GL. 1993 The final stage of the collapse of a cavitation bubble near a rigid wall. *J. Fluid Mech.* **257**, 147–181. (doi:10.1017/S0022112093003027)
7. Brennen CE. 1995 *Cavitation and bubble dynamics*. Oxford, UK: Oxford University Press.
8. Klaseboer E, Hung KC, Wang C, Wang CW, Khoo BC, Boyce P, Debono S. 2005 Experimental and numerical investigation of the dynamics of an underwater explosion bubble near a resilient/rigid structure. *J. Fluid Mech.* **537**, 378–413. (doi:10.1017/S0022112005005306)

9. Leighton TG, Cleveland RO. 2010 Lithotripsy. *Proc. Inst. Mech. Eng. H J. Eng. Med.* **224**, 317–342. (doi:10.1243/09544119JEIM588)
10. Bourne NK, Field JE. 1991 Bubble collapse and the initiation of explosion. *Proc. R. Soc. Lond. A* **435**, 423–435. (doi:10.1098/rspa.1991.0153)
11. Bourne NK, Milne JE. 2003 The temperature of shock-collapsed cavity. *Proc. R. Soc. Lond. A* **459**, 1851–1861. (doi:10.1098/rspa.2002.1101)
12. Ohl CD, Ikink R. 2003 Shock-wave-induced jetting of micron-size bubbles. *Phys. Rev. Lett.* **21**, 214502. (doi:10.1103/PhysRevLett.90.214502)
13. Tandiono T, Ow DSW, Driessen L, Chin CSH, Klaseboer E, Choo ABH, Ohl SW, Ohl CD. 2012 Sonolysis of *Escherichia coli* and *Pichia pastoris* in microfluidics. *Lab Chip.* **12**, 780–786. (doi:10.1039/C2LC20861J)
14. Birkin PR *et al.* 2015 Cold water cleaning of brain proteins, biofilm and bone—harnessing an ultrasonically activated stream. *Phys. Chem. Chem. Phys.* **17**, 20 574–20 579. (doi:10.1039/C5CP02406D)
15. Howlin RP *et al.* 2015 Removal of dental biofilms with a novel ultrasonically-activated water stream. *J. Dental Res.* **94**, 1303–1309. (doi:10.1177/0022034515589284)
16. Leighton TG. 2017 The acoustic bubble: ocean, cetacean and extraterrestrial acoustics, and cold water cleaning. *IOP J. Phys. Conf. Ser.* **797**, 012001. (doi:10.1088/1742-6596/797/1/012001)
17. Field JE. 1991 The physics of liquid impact, shock wave interactions with cavities, and the implications to shock-wave lithotripsy. *Phys. Med. Biol.* **36**, 1475–1484. (doi:10.1088/0031-9155/36/11/007)
18. Anderson PA, Hawker N, Betney M, Tully B, Ventikos Y, Roy RA. 2013 Experimental characterisation of light emission during shock-driven cavity collapse. *Proc. Mtgs. Acoust.* **19**, 075039. (doi:10.1121/1.4800761)
19. Kodama T, Takayama K. 1998 Dynamic behaviour of bubbles during extracorporeal shock-wave lithotripsy. *Ultrasound Med. Biol.* **24**, 723–738. (doi:10.1016/S0301-5629(98)00022-2)
20. Philipp A, Delius M, Scheffczyk C, Vogel A, Lauterborn W. 1993 Interaction of lithotripter-generated shock waves with air bubbles. *J. Acoust. Soc. Am.* **93**, 2496–2509. (doi:10.1121/1.406853)
21. Leighton TG, Turangan CK, Jamaluddin AR, Ball GJ, White PR. 2013 Prediction of far-field acoustic emissions from cavitation clouds during shock wave lithotripsy for development of a clinical device. *Proc. R. Soc. A* **469**, 20120538. (doi:10.1098/rspa.2012.0538)
22. Leighton TG, Fedele F, Coleman AJ, McCarthy C, Ryves S, Hurrell AM, Stefano AD, White PR. 2008 A passive acoustic device for real-time monitoring the efficacy of shockwave lithotripsy treatment. *Ultrasound Med. Biol.* **34**, 1651–1665. (doi:10.1016/j.ultrasmedbio.2008.03.011)
23. Ding Z, Gracewski SM. 1996 The behaviour of a gas cavity impacted by a weak or strong shock wave. *J. Fluid Mech.* **309**, 183–209. (doi:10.1017/S0022112096001607)
24. Nourgaliev RR, Dinh TN, Theofanous TG. 2006 Adaptive characteristics-based matching for compressible multi-fluid dynamics. *J. Comput. Phys.* **213**, 500–529. (doi:10.1016/j.jcp.2005.08.028)
25. Johnsen E, Colonius T. 2009 Numerical simulations of non-spherical bubble collapse. *J. Fluid Mech.* **629**, 231–262. (doi:10.1017/S0022112009006351)
26. Kobayashi K, Kodama T, Takahira H. 2011 Shock wave-bubble interaction near soft and rigid boundaries during lithotripsy: numerical analysis by the improved ghost fluid method. *Phys. Med. Biol.* **56**, 6421–6440. (doi:10.1088/0031-9155/56/19/016)
27. Klaseboer E, Fong SW, Turangan CK, Khoo BC, Szeri AJ, Calvisi ML, Sankin GN, Zhong P. 2007 Interaction of lithotripter shockwaves with single inertial cavitation bubbles. *J. Fluid Mech.* **593**, 33–56. (doi:10.1017/S002211200700852X)
28. Blake JR, Taib BB, Doherty G. 1986 Transient cavities near boundaries. Part 1: Rigid boundary. *J. Fluid Mech.* **170**, 479–497. (doi:10.1017/S0022112086000988)
29. Wang Q. 2015 Bubble dynamics in a compressible liquid in contact with a rigid boundary. *Interface Focus* **5**, 20150048. (doi:10.1098/rsfs.2015.0048)
30. Freund JB, Shukla RK, Evan AP. 2009 Shock-induced bubble jetting into a viscous fluid with application to tissue injury in shock-wave lithotripsy. *J. Acoust. Soc. Am.* **126**, 2746–2756. (doi:10.1121/1.3224830)
31. Xie WF, Young YL. 2007 Two-dimensional shock induced collapse of gas bubble near a semifinite deformable solid. *J. Mech. Mater. Struct.* **2**, 1881–1900. (doi:10.2140/jomms.2007.2.1881)

32. Chahine GL. 2014 Modeling of cavitation dynamics and interaction with material. In *Advanced experimental and numerical techniques for cavitation erosion prediction* (eds K-H Kim, GL Chahine, JP Franc, A Karimi), pp. 123–173. Fluid Mechanics and its Applications, vol. 106. Berlin, Germany: Springer.
33. Chahine GL, Hsiao C-T. 2015 Modeling cavitation erosion using fluid-material interaction simulations. *Interface Focus* **5**, 20150016. (doi:10.1098/rsfs.2015.0016)
34. Hsiao C-T, Jayaprakash A, Kapahi A, Choi J-K, Chahine GL. 2014 Modeling of material pitting from cavitation bubble collapse. *J. Fluid Mech.* **755**, 142–175. (doi:10.1017/jfm.2014.394)
35. Howell BP, Ball GJ. 2000 Damping of mesh-induced errors in free-Lagrange simulations of Richtmyer-Meshkov instability. *Shock Waves* **10**, 253–264. (doi:10.1007/s001930000055)
36. Howell BP, Ball GJ. 2002 A free-Lagrange augmented Godunov method for the simulation of elastic-plastic solids. *J. Comput. Phys.* **175**, 128–167. (doi:10.1006/jcph.2001.6931)
37. Turangan CK. 2004 Free-Lagrange simulations of cavitation bubble collapse. PhD thesis, University of Southampton, UK.
38. Baik K, Jiang J, Leighton TG. 2010 Acoustic attenuation, phase and group velocities in liquid-filled pipes: theory, experiment, and examples of water and mercury. *J. Acoust. Soc. Am.* **128**, 2610–2624. (doi:10.1121/1.3495943)
39. Jiang J, Baik K, Leighton TG. 2011 Acoustic attenuation, phase and group velocities in liquid-filled pipes II: simulation for spallation neutron sources and planetary exploration. *J. Acoust. Soc. Am.* **130**, 695–706. (doi:10.1121/1.3598463)
40. Leighton TG, Baik K, Jiang J. 2012 The use of acoustic inversion to estimate the bubble size distribution in pipelines. *Proc. R. Soc. A* **468**, 2461–2484. (doi:10.1098/rspa.2012.0053)
41. Ball GJ. 1996 A free-Lagrange method for unsteady compressible flow: simulation of a confined cylindrical blast wave. *Shock Waves* **5**, 311–325. (doi:10.1007/BF02425224)
42. Harten A, Lax PD, van Leer B. 1983 On upstream differencing and Godunov-type scheme for hyperbolic conservation law. *SIAM Rev.* **25**, 35–61. (doi:10.1137/1025002)
43. Flores J, Holt M. 1981 Glimm's method applied to underwater explosions. *J. Comput. Phys.* **44**, 377–387. (doi:10.1016/0021-9991(81)90058-9)
44. Dukowicz JK. 1985 A general, non-iterative Riemann solver for Godunov's method. *J. Comput. Phys.* **61**, 119–137. (doi:10.1016/0021-9991(85)90064-6)
45. Wilkins ML. 1999 *Computer simulation of dynamic phenomena*. Berlin, Germany: Springer.
46. Cunningham KB, Coleman A, Leighton TG, White PR. 2001 Characterising *in vivo* acoustic cavitation during lithotripsy with time-frequency methods. *Acoust. Bull.* **26**, 10–16.
47. Lauer E, Hu XY, Hickel S, Adams NA. 2012 Numerical modelling and investigation of symmetric and asymmetric cavitation bubble dynamics. *Comput. Fluids* **69**, 1–19. (doi:10.1016/j.compfluid.2012.07.020)
48. Church CC. 1989 A theoretial study of cavitation generated by an extracorporeal shock wave lithotripter. *J. Acoust. Soc. Am.* **86**, 215–227. (doi:10.1121/1.398328)
49. Leighton TG. 2007 What is ultrasound? *Prog. Biophys. Mol. Biol.* **93**, 3–83. (doi:10.1016/j.pbiomolbio.2006.07.026)
50. Klaseboer E, Turangan CK, Fong SW, Liu TG, Hung KC, Khoo BC. 2006 Simulations of pressure-pulse bubble interaction using boundary element method. *Comput. Methods Appl. Eng.* **195**, 4287–4302. (doi:10.1016/j.cma.2005.08.014)
51. Haller KK, Poulikakos D, Ventikos Y, Monkewits P. 2003 Shock wave formation in droplet impact on a rigid surface: lateral liquid motion and multiple wave structure in the contact line region. *J. Fluid Mech.* **490**, 1–14. (doi:10.1017/S0022112003005093)
52. Brunton JH. 1967 Erosion by liquid shock. In *Proc. 2nd Int. Conf. Rain Eros.* (eds AA Fyall, RB King), pp. 821–823. Farnborough, UK: Royal Aircraft Establishment.
53. Leighton TG. 1994 *The acoustic bubble*. London, UK: The Academic Press.
54. Leighton TG *et al.* 2005 Characterisation of measures of reference acoustic cavitation: an experimental feasibility trial. In *Bubble and particle dynamics in acoustic fields: modern trends and applications* (ed. AA Doinikov), pp. 37–94. Kerala, India: Research Signpost.
55. Johnson GR, Cook WH. 1983 A constitutive model and data for metals subjected to large strains, high strain rates and high temperatures. In *Proc. of the 7th Int. Symp. on Ballistics, The Hague, The Netherlands, 19–21 April, 1983*, pp. 541–547. The Hague, The Netherlands: International Ballistics Committee.
56. Turangan CK, Ball GJ, Jamaluddin AR, Leighton TG. 2017 Data from: Numerical studies of cavitation erosion on an elastic-plastic material caused by shock-induced bubble collapse. University of Southampton Repository. (https://doi.org/10.5258/SOTON/D0195)